Influence of Fundamental Model Uncertainties on Silicon Solar Cell Efficiency Simulations

Sven Wasmer, Andreas Fell, and Johannes M. Greulich

***Abstract*— We determine the uncertainties on simulated efficiencies of silicon solar cells due to uncertainties of the fundamental physical models. To determine these, we refit their parameters to the underlying measurement data. Using a metamodeling and Monte Carlo simulation approach, we then deduce how these propagate to the simulated solar cell efficiency. This is evaluated for 150-μm-thick 1 Ωcm p-type standard and advanced silicon passivated emitter and rear cells (PERC), as well as for an ideal silicon solar cell. When sticking to the best-known set of physical models, we determine resulting efficiency uncertainties as low as 0.06%$_{abs}$ for usual PERC cells and 0.1%$_{abs}$ for an ideal cell. In a variance-based sensitivity analysis, we find the uncertainties of the bandgap and the hole density-of-states effective mass as well as the Auger recombination in the limiting case to dominate the efficiency uncertainty. In addition to these relatively low uncertainties, larger discrepancies may arise when applying different physical models for otherwise fixed device properties. We determine comparably large efficiency discrepancies of up to 0.6%$_{abs}$ for the two most prominent bandgap narrowing (BGN) models, and up to 0.15%$_{abs}$ for the two most recent parameterizations of free carrier absorption. We also show evidence that for the specific case of a strong space charge region being present at a recombining surface, Schenk's BGN model fails to replicate experiments. Those discrepancies highlight the necessity of further research on those models. Finally, an error of up to 0.08%$_{abs}$ is observed by simplifying diffused regions on textured surfaces to a planar geometry.**

***Index Terms*— Modeling, numerical simulation, photovoltaic cells, silicon, uncertainty analysis.**

I. Introduction

MODELS for the numerical device simulations of silicon solar cells are elaborate and have been thoroughly summarized for example by Altermatt [1], and typical input parameters are given by Fell *et al.* [2]. Many of the physical model parameters are pretty accurately known, but to the authors' knowledge, no publication deals with an actual analysis of all the single model uncertainties on a derived combined uncertainty of simulated cell efficiencies.

In this paper, we therefore conduct an uncertainty analysis concerning the propagation of uncertainty of fundamental models onto the simulated solar cell efficiencies. As usual the fundamental models are specified as analytical parameterizations, where for example temperature or doping concentration dependence is reflected, uncertainties have to be considered on the model parameters. As these are seldom stated in the literature, we refit the models to the underlying measurement data in order to get access to the fit parameters' uncertainties. Furthermore, we propose a new parameterization of the hole density-of-states effective mass m_{h}^{*} that has a greater valid physical range and needs one parameter less than the polynomial model proposed in [3].

We conduct the uncertainty analysis in a metamodeling and Monte Carlo simulation approach that was introduced and applied in [4]–[6], and which was based on the work by Müller *et al.* [7] who introduced these analyses to the photovoltaics community. Here, after the uncertainties of the physical model parameters have been derived, we deduce the uncertainties of the simulated efficiencies of three types of solar cells with broadly varying efficiencies. Consequently, we determine the most influencing parameters and models, which might, therefore, be the focus of the future model refinements. We conduct all these analyses for a constant base material of 150-μm-thick boron-doped p-type silicon wafer with a resistivity of 1 Ωcm. Uncertainties of input parameters to the solar cell simulation other than the fundamental physical models, e.g., minority excess charge carrier lifetime in the bulk, emitter saturation current density, and metal grid finger width, are specific to manufacturing technology and are thus not considered in this fundamental study.

This paper is an enhanced version of one previously published in the Proceedings of the Seventh Edition of the World Conference on Photovoltaic Energy Conversion (WCPEC-7) [8]. It contains a revised analysis of the impact of the bandgap and hole density-of-states effective masses and a broader elaboration on the parameters of the examined solar cell types. Furthermore, a discussion of further uncertainties is appended, where, e.g., consistency of the models used for extracting saturation current densities on the one hand and those used

Manuscript received August 3, 2018; revised September 28, 2018; accepted November 15, 2018. This work was supported by the German Ministry for Economic Affairs and Energy through the Project "CUT-B," under Grant 0325910A. The work of S. Wasmer was supported by the State Graduate Funding Program of Baden-Württemberg. The review of this paper was arranged by Editor B. Hoex.*(Corresponding author: Sven Wasmer.)*

S. Wasmer was with the Fraunhofer Institute for Solar Energy Systems, 79110 Freiburg, Germany. He is now with Hanwha Q CELLS GmbH, 06766 Bitterfeld-Wolfen, Germany (e-mail: s.wasmer@q-cells.com).

A. Fell and J. M. Greulich are with the Fraunhofer Institute for Solar Energy Systems, 79110 Freiburg, Germany (e-mail: andreas.fell@ise.fhg.de; johannes.greulich@ise.fhg.de).

Color versions of one or more of the figures in this paper are available online at http://ieeexplore.ieee.org.

Digital Object Identifier 10.1109/TED.2018.2882776

in the cell simulation, on the other hand, is not guaranteed, and where there is more than one generally accepted model.

II. Physical Models and Their Uncertainty

In the following, we refer to the term "uncertainty" as one standard deviation of assumed Gaussian distributed measurement uncertainties with the implications, e.g., that a range of twice this values correspond to a 95% confidence interval.

In order to get full access to the fit parameters and their uncertainties, we first digitize the relevant measurement data of the mobility model for electron and holes by Klaassen [9], [10]. These data comprise the majority mobility values of electrons at 300 K ([9] for $N_\mathrm{D} = 10^{14}$–10^{19} cm^{-3} and [11] for $N_\mathrm{D} = 10^{19}$–10^{22} cm^{-3}) and holes ([12] for $N_\mathrm{A} = 10^{14}$–10^{19} cm^{-3} and [11] for $N_\mathrm{A} = 10^{19}$–10^{22} cm^{-3}) and the temperature-dependent data of Li and Thurber [13] and Li [14]. For the minority mobility data, we digitize the ones summarized by Altermatt [1] for the doping concentration dependence and for the injection dependence the ones by Hameiri *et al.* [15] for doped silicon and the ones of Dannhäuser [16] and Krausse [17] for undoped silicon, but only for $\Delta n \leq 1.3 \cdot 10^{16}$ cm^{-3}, as for higher injection conditions the temperature of the sample probably influenced the measurements [9]. We assume uncertainties of $5\%_\mathrm{rel}$ on the data points, which are estimated by their scattering. The fitting procedure is then carried out as follows. First, the majority mobility model parameters are fit to the corresponding data at 300 K and kept at these default values in the following. Then, we fit the parameters $\theta_{\mu,i}$ describing the temperature dependence of the mobility of charge carrier type i. Finally, for the minority mobility model parameters, we fit the sum of electron and hole mobilities [with relative uncertainties of $(2 \cdot 0.05^2)^{1/2} \approx 7\%$], where the corresponding majority mobility is calculated with the default majority parameters.

Regarding the other fundamental models, we use the bandgap data by Bludau *et al.* with uncertainties of 1 meV on each data point given in [18], and the hole density-of-states effective mass measured by Sproul and Green [19] that were corrected by Couderc *et al.* [3] for bandgap narrowing (BGN) in the 10 Ωcm silicon wafers and add the $T = 4.2$ K measurement by Barber [20]. The data by Misiakos and Tsamakis [21] serve only as comparative values, as they seem not to be suitable at low temperatures [3]. Concerning the electron density-of-states effective mass, we stick to the well-known parameters and their uncertainty given by Green [22]. For the Auger recombination, we estimate uncertainties of ±10% on the linear parameters C_n0, C_p0, and $C_{\Delta n}$ of the model by Richter *et al.* [23]. This simplified approach is justified by a 20% confidence interval on the underlying minority charge carrier lifetime measurements (see [24, Fig. 1]), equivalent to two standard deviations if assuming a typical 95% confidence interval and Gaussian distributed uncertainties. For the uncertainty of the silicon absorption coefficient, we adhere to the results of Schinke *et al.* [25] and later add the impact of this uncertainty (relative uncertainty of 0.035% for 150-μm-thick silicon) on cell efficiency via Gaussian propagation of uncertainty using partial derivatives.

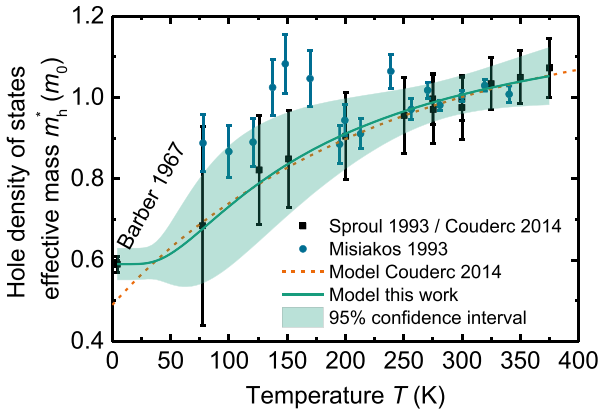

Fig. 1. Temperature dependence of hole density-of-states effective mass. Fit are the data by Barber, Sproul, and Couderc.

For the investigation of BGN and incomplete ionization (i.i.), we refer to Sections IV-A-IV-C

Regarding the hole density-of-states effective mass, we fit the following formula according to [22] to the data described earlier for 4.2 K $\leq T \leq$ 375 K:

$$m_\mathrm{h}^* = \left(m_\mathrm{h0}^{*\frac{3}{2}} + m_\mathrm{so}^{*\frac{3}{2}} \exp\left(-\frac{\Delta_\mathrm{m,h}}{kT} \right)^{\frac{3}{2}} \right)^{\frac{2}{3}} \tag{1}$$

where k is Boltzmann's constant and T is the temperature with the split-off hole band mass m_so^*, and $\Delta_\mathrm{m,h}$ is the energy difference between the energy maximum in the split-off band and the other two bands. In contrast to [22], the light and heavy hole band masses are combined to one m_h0^*, whose value is basically given by the $T = 4.2$ K measurement by Barber *et al.* [20]. With this fit, a greater temperature range is covered and one parameter less is needed than in [3]. The new fit is given in Fig. 1. It agrees very well with the fit by Couderc for temperatures greater than 50 K and with Misiakos' data for temperatures greater than 200 K.

All the fits are done with the data analysis software OriginPro 9.1G. The uncertainties s_i on the fit parameters are calculated according to [26]

$$s_i = \sqrt{C_{ii}} \quad \text{with } C = \left(F'F\right)^{-1} \text{ and } F_{ij} = \frac{1}{\sigma_j}\frac{\partial f}{\partial i} \tag{2}$$

where C_{ii} are the diagonal elements of the covariance matrix C and F is the Jacobian of the model f, where σ_j is the uncertainty of the data point j and the second term is the partial derivative of f with respect to the parameter i. Contrary to the default setting in OriginPro 9.1G, where only the relative quantities of σ_j are taken into account (C is scaled with the mean residual variance σ^2), the uncertainties of the data points are taken as absolute values in (2). We find this to agree better with uncertainties determined in Monte Carlo simulations, where each data point is varied according to its Gaussian uncertainty, and deducing the fit parameter distributions from these (see also [27]).

All the refitted parameters and those used from the literature are given in Table I together with their uncertainties. Differences in the model output parameters and the simulated

TABLE I
SUMMARY OF MODEL PARAMETERS

Model	Symbol	Unit	Value	Uncertainty (Std. deviation)
Bandgap [30]	E_{g0}	eV	1.1701	$5.2{\cdot}10^{-4}$
	α_{Eg}	eV/K	$3.2{\cdot}10^{-4}$	$4.5{\cdot}10^{-5}$
	θ_{Eg}	K	445	92
	Δ_{Eg}	-	0.5	0.1
Electron mass [22]	m_l^*	m_0	0.9163 [22]	0.0001 [22]
	m_t^*	m_0	0.1905 [22]	0.0004 [22]
Hole mass (Eq. 1)	m_{h0}^*	m_0	0.59	0.02
	m_{so}^*	m_0	1.00	0.19
	$\Delta_{m,h}$	eV	0.0101	0.0048
Electron majority mobility [9, 10]	$\theta_{\mu,e}$	-	2.218	0.037
	$\alpha_{\mu,e}$	-	0.809	0.029
	$N_{ref,1,e}$	cm^{-3}	$1.12{\cdot}10^{17}$	$1.2{\cdot}10^{16}$
	$\mu_{min,e}$	$cm^2/(Vs)$	74.74	1.95
	$\mu_{max,e}$	$cm^2/(Vs)$	1357.8	33.7
	$N_{ref,D}$	cm^{-3}	$3.421{\cdot}10^{20}$	$1.15{\cdot}10^{19}$
	c_D	-	0.1631	0.0064
Hole majority mobility [9, 10]	$\theta_{\mu,h}$	-	2.163	0.055
	$\alpha_{\mu,h}$	-	0.774	0.028
	$N_{ref,1,h}$	cm^{-3}	$2.47{\cdot}10^{17}$	$2.18{\cdot}10^{16}$
	$\mu_{min,h}$	$cm^2/(Vs)$	48.9	1.3
	$\mu_{max,h}$	$cm^2/(Vs)$	457.9	7.6
	$N_{ref,A}$	cm^{-3}	$5.2{\cdot}10^{20}$	$4.3{\cdot}10^{19}$
	c_A	-	0.69623	0.063
Minority mobility [9, 10]	m_e/m_0	-	0.81	0.10
	m_h/m_0	-	0.83	0.10
	f_{CW}	-	0.83	0.36
	f_{BH}	-	5.51	1.1
Auger recomb. [23]	C_{n0}	cm^6/s	$2.5{\cdot}10^{-31}$ [23]	$2.5{\cdot}10^{-32}$
	C_{p0}	cm^6/s	$8.5{\cdot}10^{-32}$ [23]	$8.5{\cdot}10^{-33}$
	$C_{\Delta n}$	cm^6/s	$3{\cdot}10^{-29}$ [23]	$3{\cdot}10^{-30}$

efficiencies using either the refitted or the original values are negligible.

III. UNCERTAINTY ANALYSIS

A. Examined Solar Cells

We conduct the uncertainty analysis for three different solar cells: standard and advanced passivated emitter and rear cells (PERC) with parameters from [5] for regenerated base material as well as for the limit of silicon solar cells [28]. We numerically simulate the devices at a temperature of 25 °C using Sentaurus TCAD L-2016.03 and use the experimental emitter doping profile "DiffOxImp" of [29]. For simplicity, the pitch of the front and rear contacts was set equal to 1.2 mm for the standard and 1.0 mm for the advanced PERC cell. The most notable difference of the advanced PERC cell is the lower emitter doping concentration in the passivated area modeled by virtually etching the profile by 0.1 μm (peak concentration of $2.4 \cdot 10^{20}$ cm^{-3} and p-n junction depth of 0.5 μm compared to $1.7 \cdot 10^{19}$ cm^{-3} and 0.4 μm). This results in saturation current densities of the passivated emitter $j_{0e,pass}$ of 86 and 25 fA/cm^2, respectively.

We model the local back surface field (BSF) using elliptically shaped aluminum (Al) doped regions [5] with increasing doping concentration from $1.7 \cdot 10^{18}$ to $4.6 \cdot 10^{18}$ cm^{-3} with a depth d_{BSF} of 0.75 μm in case of the standard PERC cell and $1 \cdot 10^{19}$–$1.8 \cdot 10^{19}$ cm^{-3} with $d_{BSF} = 1.5$ μm for the advanced PERC cell. The resulting saturation current densities $j_{0,BSF}$ are 1560 and 330 fA/cm^2. The relatively low d_{BSF} compared to experimentally obtained values (e.g., summarized in [2]) are explained by the neglecting of AlO defects and i.i., which does not impact the efficiency outcome when d_{BSF} is calibrated to match the experimental $j_{0,BSF}$.

Concerning the front metalized region of the standard PERC cell, the doping profile is also virtually etched back in order to replicate the high saturation current densities experimentally observed. The surface recombination velocities (SRVs) in the passivated and metalized areas are adjusted such that the resulting saturation current densities match those of [5], with metalized $j_{0e,met}$ of 1500 and 184 fA/cm^2, respectively.

For the limiting efficiency, we simulate a 1-D silicon solar cell for again a p-type base material with a resistivity of 1 Ωcm with a very lowly doped emitter with a Gaussian doping profile of 10^{17} cm^{-3} peak phosphorus concentration and p-n junction at 0.14 μm without surface recombination and assumed ideal ohmic contacts.

B. Monte Carlo Simulations

In a screening step, we first exclude noninfluencing parameters (e.g., the hole majority mobility) and vary in total 17 parameters of Table I with ±4 standard deviations in our design of experiment (DoE) and metamodeling approach [4], [5] using a Latin hypercube DoE and Gaussian process regression.

Then, in Monte Carlo simulations, care has to be taken as parameters can be correlated. These correlations can be incorporated by first drawing random numbers from the standardized (zero mean and unit variance) 1-D Gaussian distributions, resulting in an uncorrelated input matrix X. Then, the correlations are incorporated in the new matrix Z by

$$Z = LX \quad \text{with } LL^T = C \tag{3}$$

where L is the Cholesky decomposition (lower triangular matrix) of the correlation matrix C. The columns of Z are then transformed back into the real space before the Monte Carlo simulations.

We find for the simulated efficiencies: (21.50 ± 0.063)% and (23.43 ± 0.066)% for the standard and advanced PERC cell, respectively, as well as (29.18 ± 0.096)% for the limiting efficiency. Thus, we find a rather low uncertainty of the simulated energy conversion efficiency below $0.1\%_{abs}$, which is lower than the typical uncertainty caused by directly measured parameters deduced from real samples (e.g., wafer thickness, charge carrier lifetime, and SRV).

Note that these results and those of the sensitivity analysis of the next section hold only true provided the soundness of the uncertainties given in the literature.

C. Sensitivity Analysis

Fig. 2 shows the results of the variance-based sensitivity analysis as: 1) the relative contribution S_η (also known as "main effect index," as described in [31], and applied in the solar cell modeling in [4] and [6]) of the model parameter uncertainties to the total efficiency variance and 2) in terms of absolute standard deviation σ_η, for each model of Table I and the absorption coefficient [25]. Striking is the

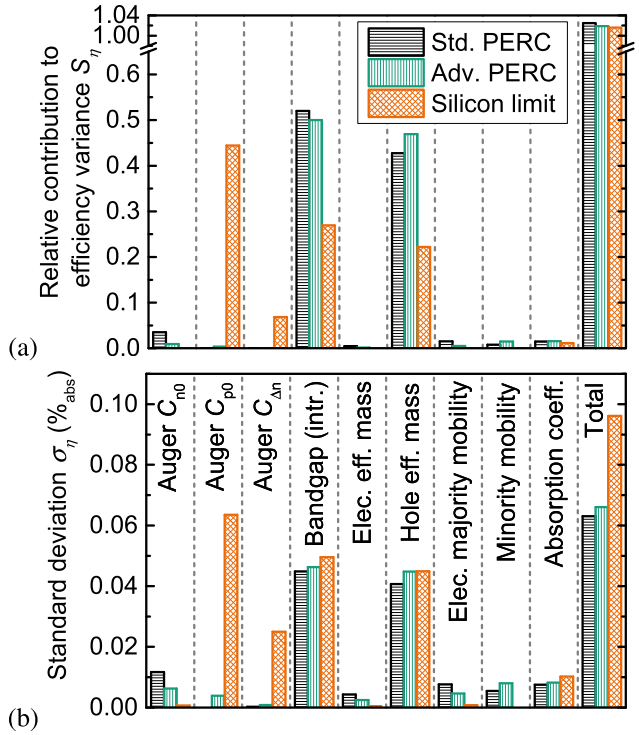

Fig. 2. (a) Relative contribution of the model parameter uncertainties to the total efficiency variance. (b) Absolute contribution in terms of standard deviation.

relatively large influence of the uncertainty of the bandgap E_g (efficiency standard deviation of $\sim$0.045%$_{abs}$) and the hole density-of-states effective mass m_h^* ($\sim$0.045%$_{abs}$) as well as of the Auger recombination model in the case of the limiting efficiency (0.068%$_{abs}$), explaining together over 98% of the observed efficiency variance for each cell type. Most of the Auger recombination in the limit is due to C_{p0} that models the recombination in the base due to the boron doping. The corresponding C_{n0} sees a decreasing influence with increasing cell level because of the reduction in emitter doping concentration. The parameter $C_{\Delta n}$ accounting for high-injection effects only has an influence in the limiting efficiency, but there in total less than C_{p0} as the injection density at the maximum power point of $\sim 2 \cdot 10^{15}$ cm^{-3} is still almost one order of magnitude lower than that of the base doping concentration of $N_A = 1.5 \cdot 10^{16}$ cm^{-3}.

Although the intrinsic bandgap model parameter uncertainties result in a standard deviation of E_g of only 0.5 meV at 298.15 °C, its impact is detrimental and can be accounted to its direct and indirect impact on the cell's voltage. The direct part is that the theoretical maximum V_{oc} is limited by the bandgap. The indirect part is due to a change in the effective intrinsic density $n_{i,eff}$, and hence, the recombination properties of the device. Equally important is m_h^*, whose uncertainty is evident from Fig. 1, and whose model parameters showed the largest relative uncertainties leading to a standard deviation of m_h^* of 0.024 m_0 at 298.15 °C. Noteworthy, a significant interaction between E_g and m_h^* is detected, explaining about 20%–30% of the total η variance and is distributed equally to E_g and m_h^* in Fig. 2. This means that interaction terms $\sim E_g \cdot m_h^*$ influence η, showing the clear benefit of the Monte Carlo simulations and a variance-based sensitivity analysis over a "classical" Gaussian propagation of uncertainty via local derivatives.

Improvements in the uncertainty of the bandgap are possibly hard to achieve, as it is currently very low (0.5%$_{rel}$). Since the Auger recombination turned out to be only relevant in the limiting case, in order to enhance the accuracy of simulations of typical PERC solar cells, it is advised to work first on the accuracy of the measurements of the hole density-of-states effective mass.

All other models show only a comparably small influence and can be considered accurate enough for typical silicon solar cell simulations.

Finally, the noteworthy higher absolute contribution of the minority mobility model uncertainty to the advanced PERC cell compared to the standard one [see Fig. 2(b)] can be explained by an increased sensitivity to the unchanged base diffusion length on this lower overall recombination level.

D. Discussion of Base Material

Note that these findings strictly only hold true for the examined base material of 150-μm-thick boron-doped p-type wafers with a specific resistance of 1 Ωcm. However, we believe that for solar cells based on n-type material or for thinner wafers (only lowering the silicon usage seems to lower photovoltaic energy conversion productions costs) the result of low overall efficiency uncertainty would remain.

In the first case, due to the higher mobility of electrons, lower doping concentrations can be used to achieve an equivalent base resistivity ($N_D = 5 \cdot 10^{15}$ cm^{-3} for 1 Ωcm). Hence, as 1 Ωcm material is already on the lower range of commonly used base resistivities and as the models behave more docile for lower doping concentrations, little influence of switching to n-type material or higher base resistivities can be expected. Only the impact of the electron and hole parameters of the Auger recombination and the majority mobility models would be reversed, but the impacts would remain similar considering the similar relative uncertainties of the corresponding parameters of Table I. Note that for n-type material, higher lifetimes than predicted by the Richter model have already been measured [32], [33], which suggest that a new parameterization of the Auger recombination in n-type silicon is to be expected.

In the case of thinner wafers, we above all expect the Auger coefficient $C_{\Delta n}$ to increase its impact due to the higher injection densities, but this only in the "ultimate efficiency limit" case. The impact of the absorption coefficient on relative efficiency uncertainty remains below 1%$_{rel}$ even for 10-μm-thin wafers [25]. Finally, the influence of the minority mobility in the base would be decreased due to a lower sensitivity to the diffusion length.

IV. Further Uncertainties

The uncertainties discussed so far apply when consistency in the models used for extracting saturation current densities and for the cell simulation is guaranteed, and where there is only one generally accepted model. Possible resulting inaccuracies and the influence of discrepancies between parameterizations/models will be discussed in the following.

Concretely, we discuss the two most prominent BGN models, the influence of the injection-dependent part of Schenk's BGN model in nonneutral regions, the impact of i.i., an inconsistency in simulating emitters on textured surfaces and compare two free carrier absorption (FCA) parameterizations.

Note that the latter two actually do not deal with the fundamental model uncertainties but rather discuss issues that arise due to typically chosen simplified optical and electrical simulation domains of emitters on textured surfaces.

For j_0 simulations conducted in Section IV-A and all of Section IV-B through Section IV-D, we use the detailed skin solver of Quokka3 [34], whereas the full cell simulation in Section IV-A and the optical simulation in Section IV-E are conducted with Sentaurus TCAD.

A. BGN 1: Comparison of Doping-Dependent Models

Not considered earlier is the uncertainty of the BGN model by Schenk [35] as this is based on numerical calculations. Nevertheless, we find big absolute efficiency deviations of $0.58\%_{abs}$, $0.39\%_{abs}$, and $0.02\%_{abs}$ for standard and advanced PERC cells and in the limit (see also Section III-A for the details on the assumed solar cells), respectively, when instead using the model by Yan and Cuevas [36], [37] for fixed doping profiles and SRVs. Note that the SRV is commonly only indirectly determined by measuring j_0 and fitting simulations, which contain already a BGN model. Applying a different BGN model in the subsequent simulations is, therefore, an actual mistake but is still shown here to provide a quantitative estimate of the related uncertainties of different BGN models. The deviations mostly result in higher emitter saturation current densities when using the model by Yan and Cuevas (standard PERC: 176 compared to 86 fA/cm^2; an SRV of $S = 0.95 \cdot 10^5$ cm/s would be needed instead of $3.5 \cdot 10^5$ cm/s for the Schenk model to achieve the same emitter saturation current density. For the advanced PERC cell, these values result in 38 compared to 25 fA/cm^2 and 1600 instead of 3300 cm/s and for the limit in 0.036 compared to 0.034 fA/cm^2). When using fixed j_0's of emitter and BSF, meaning checking the influence of BGN within the lowly doped bulk region only, the remaining deviation is negligible. The results highlight the importance of sticking to a consistent set of models for extracting SRVs from j_0 measurements and subsequently using them within the cell simulations.

B. BGN 2: Impact of Injection Dependence in Nonneutral Regions

To the authors' knowledge, still no experimental verification of the injection-dependent, also called plasma-induced, term of Schenk's BGN model is available. In the following, we discuss an example where issues arise with the full Schenk model concerning the amount of recombination within a not completely quasi-neutral region. For this end, we regard the simulation of an Al_2O_3 passivation layer with fixed charges Q_{tot} at the interface as well as an interface density D_{it} of recombination active traps with capture cross sections σ_n and σ_p. We stick to

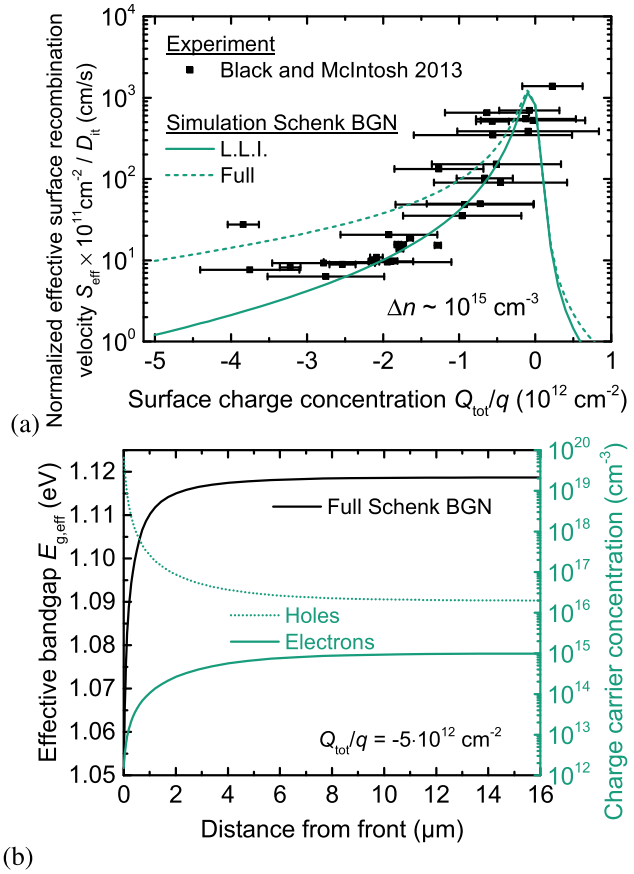

Fig. 3. (a) Comparison of simulated (lines) with measured data [38] of the effective SRV S_{eff} normalized to a midbandgap interface trap density D_{it} of 10^{11} cm^{-2}. (b) Spatial variation of the effective bandgap for the full and the L.L.I. Schenk BGN model and the charge carrier concentrations of electrons and holes.

the thorough experimental work of Black and McIntosh [38] and assume a recombination-active defect with parameters of defect A from [38, Table I]. From those, and using a peak concentration $D_{it,peak}$ of $0.8 \cdot 10^{11}$ cm^{-2}, we deduce the SRV parameters of $S_{n0} = 6490$ cm/s and $S_{p0} = 46.9$ cm/s for a midbandgap defect by integrating the Gaussian distributed defect levels. With that it is assured that D_{it} is fixed at 10^{11} cm^{-2} in the simulation for reproducing the measured, normalized to $D_{it} = 10^{11}$ cm^{-2}, effective SRVs S_{eff} for varying Q_{tot} at the surface (see [38, Fig. 7]).

While Quokka3's skin-solver directly outputs S_{eff}, it is derived from dark j–V curve simulations in Sentaurus TCAD. The excitation conditions in all cases are adjusted such that an excess charge carrier density of $\Delta n = 10^{15}$ cm^{-3} is reached in the p-type base material with a resistivity of 0.8 Ωcm as in the experiment. S_{eff} is extracted via

$$S_{eff} = \frac{j_{rec}}{q \cdot \Delta n} \tag{4}$$

where j_{rec} is the recombination current density at the interface and q is the elementary charge.

The results of the simulations for varying Q_{tot} are given in Fig. 3(a). Quite a good agreement between experiment and simulation is achieved using only the doping dependent, and hence, low-level injection (L.L.I.) part of Schenk's

BGN model. Note that there is no free parameter in the simulation, as every defect parameter is determined experimentally. The results for S_{eff} obtained by Quokka3, Sentaurus TCAD, and PC1Dmod [39] were found to agree within $15\%_{\mathrm{rel}}$.

However, we find big discrepancies when the full, plasma-induced Schenk BGN model is switched on, [see Fig. 3(a)]. Then, as can be seen in Fig. 3(b) for $Q_{\mathrm{tot}} = -5 \cdot 10^{12}$ cm^{-2}, the negative charges at the interface lead to a depletion of the density of electrons (down to $1.5 \cdot 10^{12}$ cm^{-3}) and accumulation of holes (up to $7 \cdot 10^{19}$ cm^{-3}) in the first several micrometers near the surface, and hence, to a strong BGN ($\sim$68 meV) due to the high charge density according to the plasma-induced Schenk BGN model. However, this strong BGN does not seem to describe the reality sufficiently well in such nonneutral regions and was discussed by Schenk in his original publication [35]. For the highest charge concentration of $Q_{\mathrm{tot}} = -5 \cdot 10^{12}$ cm^{-2} in Fig. 3(b), we find a ratio of the electric field times the Debye length divided by the temperature voltage of up to 1.4 and higher than 1.16 up to a depth of 10 nm. This means that quasi-neutrality is not given anymore in this region, although the order of magnitude is much lower than in space-charge regions (SCRs) of typical p-n junctions.

Concluding, it seems advantageous for simulating devices with high SCR recombination to stick to the L.L.I. BGN models, or constrain the BGN values in these regions. This is the case for highly charged passivation layers, and potentially for passivating contacts, which can introduce an equivalent situation. It is however noted that for "normal" SCRs formed, e.g., by p-n junctions, where no high recombination is present, the BGN deviations have a negligible effect on the simulated device performance.

C. Impact of Incomplete Ionization

So far, we also neglected the influence of i.i. for simplicity as on the one hand, its impact on emitter and BSF doping profiles can be bypassed by measuring the total dopant concentrations and tuning the SRV S_{emitter} in case of the emitter and, e.g., the depth d_{BSF} in case of the BSF to match the measured saturation current density. On the other hand, we find no influence of i.i. for our examined 1 Ωcm base material.

If not tuning S_{emitter} or d_{BSF} but instead simulating saturation current densities j_0 with fixed doping profiles, we find negligible j_0-differences below $3\%_{\mathrm{rel}}$ for simulations with and without incomplete ionizations models [40]–[43] for the examined emitter profiles and the highly doped BSF of the advanced PERC cell. However, for the moderately doped BSF of the standard PERC cell, we find a discrepancy in $j_{0,\mathrm{BSF}}$ of almost 70% (2570 compared to 1560 $\mathrm{fA/cm}^2$). For detailed BSF modeling, e.g., with AlO defects and using measured doping profiles, a consideration of i.i. is thus recommended. For a rough estimation of uncertainty in i.i., we vary the ground state doping energy $E_{\mathrm{dop},0}$ from 69 to 80 meV in the i.i. model proposed in [40], which should give a better fit to the measured data, but is actually physically unsound [44] and only used here to estimate an uncertainty. By comparing $j_{0,\mathrm{BSF}}$ simulations using the two $E_{\mathrm{dop},0}$ values in the i.i. model, we find a low $j_{0,\mathrm{BSF}}$ uncertainty of below $10\%_{\mathrm{rel}}$ for the standard Al-doped BSF.

In addition, the uncertainty in modeling moderately doped BSFs, i.i. can become relevant for phosphorus-doped emitters with the peak concentrations of $\sim 3 \cdot 10^{18}$ cm^{-3}, the point of maximal i.i. [43]. In these cases, the same approach of fitting the i.i. model parameters and evaluation of the impact of their uncertainty on cell efficiency could be applied. Most of the uncertainty would be due to the parameter b of the i.i. model, as it is fit to highly scattering experimental data [43]. However, we believe that the resulting efficiency uncertainty would be in the order of those determined earlier. Furthermore, the total ionized dopant fraction can in principle be measured by micro-Raman spectroscopy [44], as well as stripping hall or spreading resistance measurements [45].

D. Collection Efficiency of Emitters on Textured Surfaces

We discuss here a general problem that occurs when numerically simulating diffused regions on textured surfaces. The front side of silicon solar cells is usually textured, but due to computational issues, it is often only modeled as a planar surface in the electrical device simulation. On textured wafers, the saturation current density $j_{0\mathrm{e}}$ is higher than on planar wafers due to surface enlargement. Hence, in order to reproduce a $j_{0\mathrm{e}}$ measured on a textured surface in the planar simulation domain using an experimentally determined doping profile, the SRV S_{p0} of holes at the front side can be increased by a texture multiplier f_{tex}, accounting for the surface enlargement, resulting in an effective $S_{\mathrm{p0,eff}}$. For alkaline textured silicon with ideal pyramids, the surface enlargement factor is 1.73 [2] and serves as an orientation for f_{tex}. Dividing $S_{\mathrm{p0,eff}}$ by this factor decreases $j_{0\mathrm{e}}$ of the standard PERC cell from 86 to 63 $\mathrm{fA/cm}^2$ and from 25 to 18 $\mathrm{fA/cm}^2$ for the advanced emitter. These would be approximately $j_{0\mathrm{e}}$ on a planar surface (factor of $\sim$1.35 on the measurable quantity of $j_{0\mathrm{e}}$).

The issue with this approach is now that it underestimates the collection efficiency of charge carriers generated in the emitter, as here the actual $S_{\mathrm{p0}} = S_{\mathrm{p0,eff}}/f_{\mathrm{tex}}$ would describe the situation. Hence, the difference in collection efficiency $\eta_{\mathrm{c}}(S_{\mathrm{p0}}) - \eta_{\mathrm{c}}(S_{\mathrm{p0,eff}})$ results in an error of the short-circuit current density loss in the emitter $\Delta j_{\mathrm{sc,emitter}}$. Note that contrary to the observations of [46], overlapping of doping at the tip of the pyramid and lower concentrations in the valleys are not taken into account here and, together with possibly doping concentration-dependent S_{p0} and the surface enlargement, are rather incorporated into $S_{\mathrm{p0,eff}}$ as well while fitting to the measured $j_{0\mathrm{e}}$. The following quantitative discussion shall thus serve only as an indication of the systematic error which is often not taken into account.

Quokka3 simulations of η_{c} in the emitter are depicted in Fig. 4, and give a sense of the discrepancies by simplifying diffused regions on textured surfaces to a planar solution geometry.

Consequently, we find in the simulations short-circuit current density losses in the emitter $\Delta j_{\mathrm{sc,emitter}}$ of 0.52 and 0.37 $\mathrm{mA/cm}^2$ for effective and actual S_{p0} in case of the

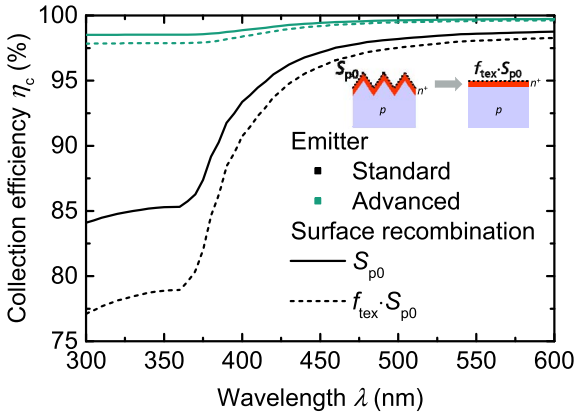

Fig. 4. Simulated wavelength-dependent collection efficiency η_C for both regarded emitters without and with applied texture multiplier of $f_{tex} = 1.7$ to the SRV of holes S_{p0} at the surface. This difference in η_C leads to the overestimation of the short-circuit current density loss in the emitter by simplifying diffused regions on textured surfaces to a planar solution geometry.

standard emitter and 0.097 and 0.066 mA/cm^2 for the advanced emitter, respectively. This means that we underestimate j_{sc} by 0.15 and 0.03 mA/cm^2 in the full cell simulation using the planar simulation domains with S_{p0} adapted for measured j_{0e} in Sentaurus TCAD (corresponding to efficiency underestimations of roughly 0.08%$_{abs}$ and 0.017%$_{abs}$). This is an effect which may become significant, e.g., when simulating selective emitters with a relatively wide highly doped region, or for double-side textured bifacial cells. Note that within the skin concept of Quokka3 j_0 and the collection efficiency of a skin are always applied as independent quantities within the boundary condition to bulk carrier transport modeling [34]. Therefore, this consistency issue is adequately addressed in Quokka3 by applying a texture multiplier to j_0 instead of S_{p0}, consequently not influencing the skin's collection efficiency.

E. Optical Modeling: Comparison of Parameterizations of Free Carrier Absorption

Finally, with different available parameterizations of the FCA, namely, the most recent parameterizations by Rüdiger *et al.* [47] and Baker-Finch *et al.* [48], an optical simulation issue is discussed here.

Rüdiger *et al.* [47] deduced their parameterization applying a simulation procedure consistent with the widely applied optical and electrical 3-D simulations using Sentaurus TCAD assuming an optical simulation symmetry element with equal doping profiles in the pyramid tips and valleys, see also the hint to [46] in Section IV-D. Possible shortcomings of this assumption are incorporated into the FCA parameterization, which, however, is then consistent when using such symmetry elements in the optical simulations.

Baker-Finch *et al.* [48] on the other hand deduced their values with a different approach that probably led to fundamentally more reliable values concerning the actual physical FCA, but could be not compatible with the mentioned common approach for optically simulating silicon solar cells.

In the optical simulations of the generation current density with AM1.5G illumination featuring pyramidically—textured surfaces and the emitter doping profile of the standard PERC cells, we find a loss of 0.18 mA/cm^2 using the parameterization of Rüdiger *et al.* [47] and 0.45 mA/cm^2 using the one by Baker-Finch *et al.* [48], a deviation of 0.27 mA/cm^2 between these two is found, leading to an estimated efficiency difference of 0.15%$_{abs}$ for standard PERC cells. This is much higher than the uncertainties above and leaves room for further research as it cannot be said generally whether the parameterization by Rüdiger *et al.* [47] underestimates FCA or whether the one by Baker-Finch *et al.* [48] overestimates it within this simulation setup.

V. Conclusion

We found that the fundamental models for p-type silicon solar cells are elaborate and allow for an accurate simulation with resulting efficiency uncertainties around 0.06%$_{abs}$ for typical PERC solar cells and around 0.1%$_{abs}$ in case of the limiting efficiency for 150-μm-thick 1 Ωcm p-type silicon excluding uncertainties of BGN and i.i. For other base doping types and concentrations as well as thicknesses, similar overall uncertainties are to be expected.

In a variance-based sensitivity analysis, it was found that the models for the bandgap (efficiency standard deviation of ∼0.045%$_{abs}$) and hole density-of-states effective mass (∼0.045%$_{abs}$), as well as the Auger recombination in the limiting case (0.068%$_{abs}$), share the biggest parts in cell efficiency variance with combined over 98% for each cell type.

In a discussion of further uncertainties, where, e.g., consistency in the models used for extracting saturation current densities and in the cell simulation is not guaranteed, and where there are more than one generally accepted model, a comparison of the two most prominent BGN models showed a comparably large effect of up to a factor of 2 on saturation current densities, and hence, of up to 0.6%$_{abs}$ on efficiency for fixed doping profiles and SRVs.

We also identified in the simulations of a passivation layer with fixed charges the full, plasma-induced BGN model by Schenk to seem not be able to describe high recombination in nonneutral regions adequately.

Incomplete ionization is found to pose a minor influence on the examined emitters and the highly doped local BSF of the advanced PERC cell. However, it can become relevant when simulating phosphorus-doped emitters with the peak concentrations of $\sim 3 \cdot 10^{18}$ cm^{-3} or a detailed modeling of moderately doped BSFs.

In an examination of a common issue regarding the simulation of diffused regions on textured surfaces, we found underestimations of the short-circuit current density of up to 0.15 mA/cm^2, and hence, up to 0.08%$_{abs}$ in efficiency due to using an effective SRV. This error could become more significant in the case of a selective emitter with wide heavily doped regions, as well as in bifacial cells with a textured rear side.

Comparing the most recent parameterizations of the FCA, we found them resulting in generation current densities discrepancies of up to 0.27 mA/cm^2, and hence, also a comparably large effect of efficiency of 0.15%$_{abs}$ for standard PERC solar cells.

Concluding, for enhancing the accuracy of simulations of typical PERC solar cells, it is advised to work first on the accuracy of the measurements for the fundamental model of the hole density-of-states effective mass.

We also highlight the necessity for a consistent usage of BGN models and for further research on the discrepancies between the theoretical model by Schenk [35] and the experimental data by Yan and Cuevas [36], [37], e.g., by measuring the bandgap of highly doped silicon wafers directly applying wavelength-modulation spectroscopy as in [18].

Concerning simulating nonneutral regions with high recombination, we recommend sticking to the L.L.I. BGN models or constraining the BGN values in these regions.

Finally, when the simulating emitters on textured surfaces, attention has to be paid concerning FCA in the optical simulations and correctly assessing the collection efficiency in the electrical simulations. These could be addressed by incorporating dopant inhomogeneities [46] into the ray tracing geometry and nonplanar surfaces into the electrical simulations as was, e.g., done in [49].

Acknowledgment

The authors would like to thank L. E. Black from the Australian National University, Canberra, ACT, Australia, for fruitful discussions and providing the raw data of Fig. 3(a).

References

[1] P. P. Altermatt, "Models for numerical device simulations of crystalline silicon solar cells—A review," *J. Comput. Electron.*, vol. 10, no. 3, pp. 314–330, 2011, doi: 10.1007/s10825-011-0367-6.

[2] A. Fell *et al.*, "Input parameters for the simulation of silicon solar cells in 2014," *IEEE J. Photovolt.*, vol. 5, no. 4, pp. 1250–1263, Jul. 2015, doi: 10.1109/jphotov.2015.2430016.

[3] R. Couderc, M. Amara, and M. Lemiti, "Reassessment of the intrinsic carrier density temperature dependence in crystalline silicon," *J. Appl. Phys.*, vol. 115, no. 9, p. 093705, 2014, doi: 10.1063/1.4867776.

[4] S. Wasmer *et al.*, "Impact of material and process variations on the distribution of multicrystalline silicon PERC cell efficiencies," *IEEE J. Photovolt.*, vol. 7, no. 1, pp. 118–128, 2017. [Online]. Available: https://ieeexplore.ieee.org/document/7756665, doi: 10.1109/JPHOTOV.2016.2626145.

[5] S. Wasmer, A. A. Brand, and J. M. Greulich, "Metamodeling of numerical device simulations to rapidly create efficiency optimization roadmaps of monocrystalline silicon PERC cells," *Energy Procedia*, vol. 124, pp. 207–214, Sep. 2017, doi: 10.1016/j.egypro.2017.09.312.

[6] S. Wasmer and J. Greulich, "Modelling and analysis of solar cell efficiency distributions," *Jpn. J. Appl. Phys.*, vol. 56, no. 8S2, p. 08MB02, 2017, doi: 10.7567/JJAP.56.08MB02.

[7] M. Müller, P. P. Altermatt, H. Wagner, and G. Fischer, "Sensitivity analysis of industrial multicrystalline PERC silicon solar cells by means of 3-D device simulation and metamodeling," *IEEE J. Photovolt.*, vol. 4, no. 1, pp. 107–113, Jan. 2014, doi: 10.1109/jphotov.2013.2287753.

[8] S. Wasmer, A. Fell, and J. M. Greulich, "Impact of uncertainties of fundamental models on simulated silicon solar cell efficiencies," in *Proc. 7th World Conf. Photovolt. Energy Convers. (WCPEC-7)*, 2018. [Online]. Available: https://www.pvsc-proceedings.org

[9] D. B. M. Klaassen, "A unified mobility model for device simulation—I. Model equations and concentration dependence," *Solid-State Electron.*, vol. 35, no. 7, pp. 953–959, 1992, doi: 10.1016/0038-1101(92)90325-7.

[10] D. B. M. Klaassen, "A unified mobility model for device simulation—II. Temperature dependence of carrier mobility and lifetime," *Solid-State Electron.*, vol. 35, no. 7, pp. 961–967, 1992, doi: 10.1016/0038-1101(92)90326-8.

[11] G. Masetti, M. Severi, and S. Solmi, "Modeling of carrier mobility against carrier concentration in arsenic-, phosphorus-, and boron-doped silicon," *IEEE Trans. Electron Devices*, vol. 30, no. 7, pp. 764–769, Jul. 1983, doi: 10.1109/T-ED.1983.21207.

[12] W. R. Thurber, R. L. Mattis, Y. M. Liu, and J. J. Filliben, "Resistivity-dopant density relationship for boron-doped silicon," *J. Electrochem. Soc.*, vol. 127, no. 10, pp. 2291–2294, 1980.

[13] S. S. Li and W. R. Thurber, "The dopant density and temperature dependence of electron mobility and resistivity in n-type silicon," *Solid-State Electron.*, vol. 20, no. 7, pp. 609–616, 1977, doi: 10.1016/0038-1101(77)90100-9.

[14] S. S. Li, "The dopant density and temperature dependence of hole mobility and resistivity in boron doped silicon," *Solid-State Electron.*, vol. 21, no. 9, pp. 1109–1117, 1978, doi: 10.1016/0038-1101(78)90345-3.

[15] Z. Hameiri, F. Rougieux, R. Sinton, and T. Trupke, "Contactless determination of the carrier mobility sum in silicon wafers using combined photoluminescence and photoconductance measurements," *Appl. Phys. Lett.*, vol. 104, no. 7, p. 073506, 2014, doi: 10.1063/1.4865804.

[16] F. Dannhäuser, "Die abhängigkeit der trägerbeweglichkeit in silizium von der konzentration der freien ladungsträger—I," *Solid State Electron*, vol. 15, no. 12, pp. 1371–1375, 1972, doi: 10.1016/0038-1101(72)90131-1.

[17] J. Krausse, "Die abhängigkeit der trägerbeweglichkeit in silizium von der konzentration der freien ladungsträger—II," *Solid-State Electron.*, vol. 15, no. 12, pp. 1377–1381, 1972, doi: 10.1016/0038-1101(72)90132-3.

[18] W. Bludau, A. Onton, and W. Heinke, "Temperature dependence of the band gap of silicon," *J. Appl. Phys.*, vol. 45, no. 4, pp. 1846–1848, 1974, doi: 10.1063/1.1663501.

[19] A. B. Sproul and M. A. Green, "Intrinsic carrier concentration and minority-carrier mobility of silicon from 77 to 300 K," *J. Appl. Phys.*, vol. 73, no. 3, pp. 1214–1225, 1993, doi: 10.1063/1.353288.

[20] H. D. Barber, "Effective mass and intrinsic concentration in silicon," *Solid-State Electron.*, vol. 10, no. 11, pp. 1039–1051, 1967, doi: 10.1016/0038-1101(67)90122-0.

[21] K. Misiakos and D. Tsamakis, "Accurate measurements of the silicon intrinsic carrier density from 78 to 340 K," *J. Appl. Phys.*, vol. 74, no. 5, pp. 3293–3297, 1993, doi: 10.1063/1.354551.

[22] M. A. Green, "Intrinsic concentration, effective densities of states, and effective mass in silicon," *J. Appl. Phys.*, vol. 67, no. 6, pp. 2944–2954, 1990, doi: 10.1063/1.345414.

[23] A. Richter, S. W. Glunz, F. Werner, J. Schmidt, and A. Cuevas, "Improved quantitative description of Auger recombination in crystalline silicon," *Phys. Rev. B, Condens. Matter*, vol. 86, no. 16, p. 165202, 2012, doi: 10.1103/PhysRevB.86.165202.

[24] A. Richter, F. Werner, A. Cuevas, J. Schmidt, and S. W. Glunz, "Improved parameterization of Auger recombination in silicon," *Energy Procedia*, vol. 27, pp. 88–94, Aug. 2012, doi: 10.1016/j.egypro.2012.07.034.

[25] C. Schinke *et al.*, "Uncertainty analysis for the coefficient of band-to-band absorption of crystalline silicon," *AIP Adv.*, vol. 5, no. 6, p. 67168, 2015, doi: 10.1063/1.4923379.

[26] W. H. Press and W. T. Vetterling, *Numerical Recipes in C*, 2nd ed. Cambridge, U.K.: Cambridge Univ. Press, 1999.

[27] P. H. Richter, "Estimating errors in least-squares fitting," *Telecommun. Data Acquisition Rep.*, vol. 42, no. 122, pp. 107–137, 1995. [Online]. Available: https://ntrs.nasa.gov/search.jsp?R=19960009481

[28] A. Richter, M. Hermle, and S. W. Glunz, "Reassessment of the limiting efficiency for crystalline silicon solar cells," *IEEE J. Photovolt.*, vol. 3, no. 4, pp. 1184–1191, Oct. 2013, doi: 10.1109/JPHOTOV.2013.2270351.

[29] S. Werner *et al.*, "Process optimization for the front side of P-type silicon solar cells," in *Proc. 29th Eur. Photovolt. Sol. Energy Conf. Exhib.*, pp. 1342–1347, 2014, doi: 10.4229/EUPVSEC20142014-2CV.4.25.

[30] R. Pässler, "Semi-empirical descriptions of temperature dependences of band gaps in semiconductors," *Phys. Status Solidi (b)*, vol. 236, no. 3, pp. 710–728, 2003, doi: 10.1002/pssb.200301752.

[31] A. Saltelli *et al.*, "Variance-based methods," in *Global Sensitivity Analysis. The Primer*. Hoboken, NJ, USA: Wiley, 2008, pp. 155–167 and 155–182, doi: 10.1002/9780470725184.ch4.

[32] Y. Wan, K. R. McIntosh, A. F. Thomson, and A. Cuevas, "Low surface recombination velocity by low-absorption silicon nitride on c-Si," *IEEE J. Photovolt.*, vol. 3, no. 1, pp. 554–559, Jan. 2013, doi: 10.1109/JPHOTOV.2012.2215014.

[33] B. A. Veith-Wolf and J. Schmidt, "Unexpectedly high minority-carrier lifetimes exceeding 20 ms measured on 1.4-Ω cm N-type silicon wafers," *Phys. Status Solidi RRL*, vol. 11, no. 11, p. 1700235, 2017, doi: 10.1002/pssr.201700235.

[34] A. Fell, J. Schön, M. C. Schubert, and S. W. Glunz, "The concept of skins for silicon solar cell modeling," *Sol. Energy Mater. Sol. Cells*, vol. 173, pp. 128–133, Dec. 2017, doi: 10.1016/j.solmat.2017.05.012.

[35] A. Schenk, "Finite-temperature full random-phase approximation model of band gap narrowing for silicon device simulation," *J. Appl. Phys.*, vol. 84, no. 7, pp. 3684–3695, 1998, doi: 10.1063/1.368545.

[36] D. Yan and A. Cuevas, "Empirical determination of the energy band gap narrowing in highly doped n^+ silicon," *J. Appl. Phys.*, vol. 114, no. 4, p. 044508, 2013, doi: 10.1063/1.4816694.

[37] D. Yan and A. Cuevas, "Empirical determination of the energy band gap narrowing in p^+ silicon heavily doped with boron," *J. Appl. Phys.*, vol. 116, no. 19, p. 194505, 2014, doi: 10.1063/1.4902066.

[38] L. E. Black and K. R. McIntosh, "Modeling recombination at the Si–Al_2O_3 interface," *IEEE J. Photovolt.*, vol. 3, no. 3, pp. 936–943, Jul. 2013, doi: 10.1109/JPHOTOV.2013.2247464.

[39] H. Haug and J. Greulich, "PC1Dmod 6.2—Improved simulation of c-Si devices with updates on device physics and user interface," *Energy Procedia*, vol. 92, pp. 60–68, Aug. 2016, doi: 10.1016/j.egypro.2016.07.010.

[40] H. Steinkemper, P. P. Altermatt, and M. Hermle, "Physically sound parameterization of incomplete ionization in aluminum-doped silicon," *AIP Adv.*, vol. 6, no. 12, p. 125202, 2016, doi: 10.1063/1.4971155.

[41] P. P. Altermatt, A. Schenk, B. Schmithüsen, and G. Heiser, "A simulation model for the density of states and for incomplete ionization in crystalline silicon. II. Investigation of Si:As and Si:B and usage in device simulation," *J. Appl. Phys.*, vol. 100, no. 11, p. 113715, 2006. [Online]. Available: https://aip.scitation.org/doi/full/10.1063/1.2386935, doi: 10.1063/1.2386935.

[42] P. P. Altermatt, A. Schenk, B. Schmithüsen, and G. Heiser, "Impact of incomplete ionisation on measurements of sheet resistivity and of carrier mobility in c-Si solar cells at room temperature," in *Proc. 20th EU PVSEC*, Barcelona, Spain, Jun. 2005, pp. 1267–1270.

[43] P. P. Altermatt, A. Schenk, and G. Heiser, "A simulation model for the density of states and for incomplete ionization in crystalline silicon. I. Establishing the model in Si:P," *J. Appl. Phys.*, vol. 100, no. 11, p. 113714, 2006, doi: 10.1063/1.2386934.

[44] H. Steinkemper *et al.*, "Adapted parameterization of incomplete ionization in aluminum-doped silicon and impact on numerical device simulation," *J. Appl. Phys.*, vol. 117, no. 7, p. 074504, 2015, doi: 10.1063/1.4913255.

[45] S. Werner *et al.*, "Doping- and carrier concentration profile characterisation of highly phosphorus-doped emitters," in *Proc. 25th EU PVSEC*, Valencia, Spain, 2010, pp. 1942–1947.

[46] H. Wagner *et al.*, "Analyzing emitter dopant inhomogeneities at textured Si surfaces by using 3D process and device simulations in combination with SEM imaging," in *Proc. IEEE Photovolt. Spec. Conf.*, Jun. 2012, pp. 313–316, doi: 10.1109/PVSC.2012.6317625.

[47] M. Rüdiger, J. Greulich, A. Richter, and M. Hermle, "Parameterization of free carrier absorption in highly doped silicon for solar cells," *IEEE Trans. Electron Devices*, vol. 60, no. 7, pp. 2156–2163, Jul. 2013, doi: 10.1109/ted.2013.2262526.

[48] S. C. Baker-Finch, K. R. McIntosh, D. Yan, K. C. Fong, and T. C. Kho, "Near-infrared free carrier absorption in heavily doped silicon," *J. Appl. Phys.*, vol. 116, no. 6, p. 063106, 2014, doi: 10.1063/1.4893176.

[49] P. Procel *et al.*, "Opto-electrical modelling and optimization study of a novel IBC c-Si solar cell," *Prog. Photovolt., Res. Appl.*, vol. 25, no. 6, pp. 452–469, 2017, doi: 10.1002/pip.2874.

Authors' photographs and biographies not available at the time of publication.